Accepted as Paper AIAA-2006-6750 at the AAS/AIAA Astrodynamics Specialist Conference, Keystone, CO, August, 2006

Repeat Ground Track Lunar Orbits in the Full-Potential Plus Third-Body Problem

Version: June 2, 2006

Ryan P. Russell*
Jet Propulsion Laboratory, Pasadena, California 91109

Martin Lara†
Real Observatorio de la Armada, San Fernando, Spain

A high degree and order Lunar gravitational field is superimposed on the Earth-Moon Restricted Three Body model to capture the dominating forces on a spacecraft in the vicinity of the Moon. For the synchronously rotating Moon, periodic orbits in this model map repeat ground tracks and represent higher order solutions to the frozen orbit problem. The near-circular, stable or near-stable solutions are found over a wide range of defining characteristics making them suitable for long-lifetime parking applications such as science orbits, crew exploration vehicle parking orbits, and global coverage constellation orbits. A full ephemeris is considered for selected orbits to evaluate the validity of the time-invariant, simplified model. Of the most promising results are the low-altitude families of near-circular, inclined orbits that maintain long-term stability despite the highly non-spherical Lunar gravity. The method is systematic and enables rapid design and analysis of long-life orbits around any tidally-locked celestial body with an arbitrarily high degree and order spherical harmonic gravity field.

I. Introduction

With the recent interest in the return trips to the Moon [1], trajectory designers are faced with a variety of challenges. The proposed missions are likely to require extended stays and global communication coverage. Therein lays the challenge to find long-lifetime orbits in the vicinity of the Moon. Traditionally, mission designers seek orbits that are "frozen" [2,3,4,5,6,7,8,9,10,11,12] with regard to the eccentricity and argument of periapse as these highly coupled orbital elements generally have secular drifts due to the third body and non-spherical gravity perturbations. Of course a secular drift in eccentricity leads directly to an impact orbit.

The frozen orbits are generally found by seeking equilibrium solutions to an averaged or reduced system. In some cases, such as the near-circular two-body zonal problem, closed form analytic series solutions are available [2] while most approaches require some form of numeric root-finding. In general however, the averaging procedure is essential, and the mathematics can be tedious and require "extensive algebraic manipulations" as pg. 40 of Ref. [7] self-describes. The complexity of the application and use of the resulting methods can be prohibitive for general use in preliminary space mission design. Furthermore, many of the higher-order effects are lost in the averaging or intentionally discarded through simplified models.

References [2,5,8] represent significant progress in terms of simplifying the procedural effort required to find frozen orbits yet both remain limited to the two-body zonal problem, as is Ref. [7]. References [2,8] operate on the averaged system and are limited to orbits of low eccentricity while Ref. [5] operates on the unaveraged system and is valid for all eccentricities. The still higher order effects of the third-body perturbations and the full gravitational potential including the non-zonal terms are yet to be investigated in the general frozen orbit problem. Clearly the relative importance of each of these higher order terms is highly dependent on spacecraft altitude. However, the impressive speeds of modern computing enable the inclusion of both higher order effects with little penalty in terms

* Member Technical Staff, Guidance, Navigation, and Control, 4800 Oak Grove Drive, M/S 301-140L, Member AIAA, email: Ryan.Russell@jpl.nasa.gov
† Commander, Ephemerides Section, 11110 San Fernando, Member AIAA, email: mlara@roa.es

of usability to the designer. The resulting dynamical system is therefore valid for a broad range of spacecraft altitudes. This higher order force model and the ability to systematically find long-life orbits therein have immediate applications for rapid trajectory design accross a wide spectrum of destinations. Examples include the Moon, Earth, Mars, Venus, and high science priority planetary moon systems such as Jupiter-Europa and Saturn-Enceladus.

In this paper, techniques based on the recent design of long-life science orbits at Europa [13,14,15] are extended to specifically find long-life orbits at the Moon. In particular, periodic orbits are sought in the Restricted Three Body Model of the Earth-Moon system plus a high resolution Lunar gravity field. The Moon's rotational period is assumed to be synchronously locked with its orbital period; thus, the periodic orbits are indeed repeat ground track (RGT) orbits.

The concept of studying RGT orbits as true periodic orbits in an unaveraged model was first explored in detail in Ref. [16] and specifically applied to low-order gravity fields in the two-body Earth problem in Ref. [17] and later in the three-body Europa problem in Ref. [13]. Repeat ground track orbits are useful for many different missions, including mapping missions when the repeat cycle is long enough. Previous research shows that periodic orbits of simplified models generally remain as RGT orbits in full ephemeris models [13,14,15,17]. However, this does not apply to the "lumpy" Moon where it has been shown that lower order zonals, particularly J_7, notably affect the long-term behavior of low altitude orbits [5]. The analysis in Ref. [3] supported by comments in Ref. [18] suggests that a 50 degree and order gravity field is necessary for accurate modeling of low-altitude Lunar orbits. Therefore, in this paper a 50x50 Lunar gravitational field is considered in order to capture the dominating higher order effects.

For simple resonances, or RGT cycles, the near-polar, near-circular solutions of the perturbed three-body problem are found to be linearly stable for altitudes less than ~1200 km. At the higher altitudes, the families evolve into stable moderately-inclined eccentric orbits. Solutions are documented for altitudes up to ~2 Moon radii. The stable or near-stable families of solutions are shown to exist for a full range of average inclinations and altitudes making them suitable for long-lifetime parking applications such as science orbits, crew exploration vehicle parking orbits, and global coverage constellation orbits [11,12]. A full ephemeris is considered for selected orbits to evaluate the validity of the time-invariant, simplified model. Because the invariant model accurately represents the Lunar gravity but only approximates the Earth's gravity and ignores all other forces, the solutions from the invariant model map to the ephemeris model more favorably as the altitude is decreased. Accordingly, the lower-altitude ephemeris propagations enjoy the same long-life stability as predicted by the invariant model. While the focus of the current application is on the Moon, the methods and accompanying software are developed generally so as to immediately apply to other bodies of interest.

II. Dynamical Models

The Earth's third body effect is modeled using the Restricted Three Body Problem (RTBP) that assumes the Earth and Moon orbit their common center of mass with a constant radius (in reality the radius varies ±5.5%). The equations are normalized such that the separation is one length unit (LU) and the orbit period is 2π time units (TU). Given the additional assumption that the rotation of the Moon is synchronous with its orbital period (in reality there is $\pm 8^{o}$ libration), the Moon-fixed reference frame is identical to the Moon centered RTBP frame depicted in Figure 1. Note that the International Astronomical Union (IAU) defined prime meridian and pole point in the direction of the Earth and the system angular momentum respectively. Both the tidal force field and the non-spherical force field are static in this rotating frame.

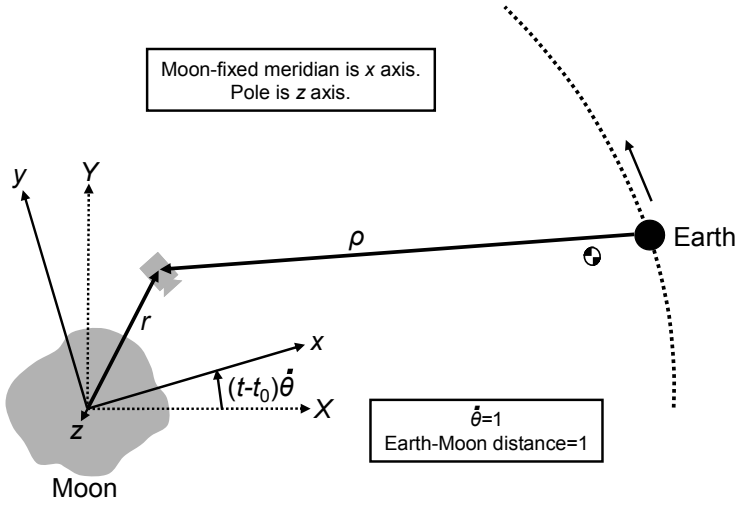

Figure 1. Moon-centered Restricted Three Body model plus full Lunar gravity field. For the synchronously rotating Moon, the (*xyz*) reference frame is coincident with the body-fixed Moon frame. Uppercase (*XYZ*) is the non-rotating frame.

The equations of motion for the rotating frame are given as

$$d\mathbf{X}/dt = \mathbf{f}(\mathbf{X}) \tag{1}$$

$$\mathbf{X} = \begin{bmatrix} x & y & z & u & v & w \end{bmatrix}^{\mathrm{T}}$$

$$\mathbf{f} = \begin{bmatrix} u \\ v \\ w \\ 2v + \partial\Omega/\partial x \\ -2u + \partial\Omega/\partial y \\ \partial\Omega/\partial z \end{bmatrix} \tag{2}$$

where a potential function, Ω, is introduced,

$$\begin{aligned} \Omega &= (x-1+\mu)^2/2 + y^2/2 + (1-\mu)/\rho + (\mu/r + U) \\ \mu &= Gm_r/(Gm_\rho + Gm_r) \\ \rho &= \sqrt{(x-1)^2 + y^2 + z^2} \\ r &= \sqrt{x^2 + y^2 + z^2} \end{aligned} \tag{3}$$

The Moon and Earth gravitational parameters are Gm_r and Gm_ρ respectively. U is the contribution due to the non-spherical Moon and is expressed via the standard spherical harmonic expansion as

$$U = -\frac{\mu}{r}\sum_{n=2}^{\infty} J_n \left(\frac{R}{r}\right)^n P_n(\sin\phi) \quad + \quad \frac{\mu}{r}\sum_{n=2}^{\infty}\sum_{m=1}^{n}\left(\frac{R}{r}\right)^n \left(C_{n,m}\cos m\lambda + S_{n,m}\sin m\lambda\right) P_{n,m}(\sin\phi) \tag{4}$$

where

$$\begin{aligned} &\sin\phi = z/r \\ &\sin\lambda = y/\sqrt{x^2+y^2}, \quad \sin m\lambda = 2\cos\lambda\sin(m-1)\lambda - \sin(m-2)\lambda \\ &\cos\lambda = x/\sqrt{x^2+y^2}, \quad \cos m\lambda = 2\cos\lambda\cos(m-1)\lambda - \cos(m-2)\lambda \end{aligned} \tag{5}$$

J_n, $C_{n,m}$, and $S_{n,m}$ are the numerical coefficients that parameterize the gravity field. The J_n terms are commonly called the zonal coefficients. P_n is n^{th} degree Legendre Polynomial and is recursively defined in Eq (6).

$$P_n(\sin\phi) = \frac{2n-1}{n}\sin\phi P_{n-1}(\sin\phi) - \frac{n-1}{n}P_{n-2}(\sin\phi)$$
$$P_0(\sin\phi) = 1, \quad P_1(\sin\phi) = \sin\phi \tag{6}$$

$P_{n,m}$ is n^{th} degree and m^{th} order associated Legendre function of the first kind and is recursively defined in Eqs. (7) and (8).

$$P_{m,m}(\sin\phi) = (2m-1)\cos\phi P_{m-1,m-1}(\sin\phi)$$
$$P_{1,1}(\sin\phi) = \cos\phi \tag{7}$$

$$\text{for } n \neq m, \quad P_{n,m}(\sin\phi) = \frac{2n-1}{n-m}\sin\phi P_{n-1,m}(\sin\phi) - \frac{n+m-1}{n-m}P_{n-2,m}(\sin\phi) \tag{8}$$

For the practical computations, the gradient of U is simpler if performed in the spherical coordinates and rotated back to the body-fixed frame as shown in Eq. (9). The gradient equations are left out for brevity. The presented equations are summarized from Ref. [19]. For more details on the spherical harmonic expressions see Refs. [19,20].

$$\begin{bmatrix} \partial U/\partial x \\ \partial U/\partial y \\ \partial U/\partial z \end{bmatrix} = \begin{bmatrix} \cos\phi\cos\lambda & -\sin\lambda & -\sin\phi\cos\lambda \\ \cos\phi\sin\lambda & \cos\lambda & -\sin\phi\sin\lambda \\ \sin\phi & 0 & \cos\phi \end{bmatrix} \begin{bmatrix} \partial U/\partial r \\ (1/r\cos\phi)\partial U/\partial\lambda \\ (1/r)\partial U/\partial\phi \end{bmatrix} \tag{9}$$

The system is Hamiltonian and admits an integral of motion, C, given in Eq. (10).

$$C = 2\Omega - \left(u^2 + v^2 + w^2\right) \tag{10}$$

For conversion to classical orbital elements, the rotating frame is defined to be aligned with the non-rotating frame at $t = t_0$ (see Figure 1) and the transformation into the non-rotating frame is given in Eq. (11).

$$\begin{bmatrix} X & Y & Z \end{bmatrix}^{\mathrm{T}} = \mathbf{R}\begin{bmatrix} x & y & z \end{bmatrix}^{\mathrm{T}}$$
$$\begin{bmatrix} U & V & W \end{bmatrix}^{\mathrm{T}} = \mathbf{R}\begin{bmatrix} u & v & w \end{bmatrix}^{\mathrm{T}} + \begin{bmatrix} 0 & 0 & 1 \end{bmatrix}^{\mathrm{T}} \times \begin{bmatrix} x & y & z \end{bmatrix}^{\mathrm{T}} \qquad \mathbf{R} = \begin{bmatrix} \cos(t-t_0) & -\sin(t-t_0) & 0 \\ \sin(t-t_0) & \cos(t-t_0) & 0 \\ 0 & 0 & 1 \end{bmatrix} \tag{11}$$

The spherical harmonic representation of the Lunar gravity field is taken from the publicly available* lp150q model, a 150x150 degree solution produced by the Lunar Prospector Gravity Science Team led by A.S. Konopliv at the Jet Propulsion Laboratory. The estimation includes all available data from past American missions to the Moon. Permanent tide adjustments of ΔJ_2 = 9.32206780233229E-08 and $\Delta C_{2,2}$ = 4.66066496097581E-08 are required. A 4x4 subset of the normalized gravity field including the adjustments is given in Eq. (12). Equation (13) gives the conversion between the normalized and un-normalized coefficients. For purposes of this study, it is emphasized that the Lunar gravity field includes the 50x50 truncated version of the lp150q model. Table 1 provides the mass and distance parameters specific to the Earth-Moon system.

* URL: http://pds-geosciences.wustl.edu/geodata/lp-l-rss-5-gravity-v1/lp_1001/sha/jgl150q1.lbl [cited 12 Mar 2006]
URL: http://pds-geosciences.wustl.edu/geodata/lp-l-rss-5-gravity-v1/lp_1001/sha/jgl150q1.sha [cited 12 Mar 2006]

$$
\begin{array}{lll}
\bar{J}_2 = 0.909427845027\text{E-}04 & \bar{C}_{3,3} = 0.122862645044\text{E-}04 & \bar{S}_{3,1} = 0.546307860882\text{E-}05 \\
\bar{J}_3 = 0.320307167959\text{E-}05 & \bar{C}_{4,1} = -0.600061939740\text{E-}05 & \bar{S}_{3,2} = 0.488913911795\text{E-}05 \\
\bar{J}_4 = -0.321409545028\text{E-}05 & \bar{C}_{4,2} = -0.709370101544\text{E-}05 & \bar{S}_{3,3} = -0.178246270720\text{E-}05 \\
\bar{C}_{2,1} = -0.186273608184\text{E-}08 & \bar{C}_{4,3} = -0.135880466594\text{E-}05 & \bar{S}_{4,1} = 0.165955644727\text{E-}05 \\
\bar{C}_{2,2} = 0.347098301319\text{E-}04 & \bar{C}_{4,4} = -0.602939150193\text{E-}05 & \bar{S}_{4,2} = -0.678562735558\text{E-}05 \\
\bar{C}_{3,1} = 0.263418358622\text{E-}04 & \bar{S}_{2,1} = -0.142453894610\text{E-}08 & \bar{S}_{4,3} = -0.134332571737\text{E-}04 \\
\bar{C}_{3,2} = 0.141853316786\text{E-}04 & \bar{S}_{2,2} = 0.144063503540\text{E-}07 & \bar{S}_{4,4} = 0.393525694440\text{E-}05
\end{array} \tag{12}
$$

$$
\begin{aligned}
J_n &= \Upsilon_n \bar{J}_n & \Upsilon_n &= \sqrt{(2n+1)} \\
C_{n,m} &= \Pi_{n,m} \bar{C}_{n,m} & \Pi_{n,m} &= \sqrt{2(2n+1)(n-m)!/(n+m)!}
\end{aligned} \tag{13}
$$

For selected ephemeris propagations, the positions, velocities, and orientations of the planets and the Moon are provided by the DE405 and pck00008.tpc estimated solutions and are publicly available* from the Jet Propulsion Laboratory [21]. The poles and prime meridians for the Earth and Moon are based on the most recent data from the IAU Working Group on Cartographic Coordinates and Rotational Elements of the Planets and Satellites [22]. The Lunar gravity model is the same as used in the simplified model while the only non-spherical term considered for the Earth is J_2=0.0010826. The active bodies for the ephemeris model include the Sun, the Moon, and all planets except Pluto.

Table 1. Earth and Moon Parameters

Parameter	*Symbol*	*Value*
Moon gravitational parameter	Gm_r	4,902.801076 km^3/s^2
Earth gravitational parameter	Gm_p	398,600.4415 km^3/s^2
Mass ratio (derived)	μ	0.01215058655960256
Moon mean radius [a]	R	1738.0 km
Earth-Moon distance (length unit)	LU	384,400 km
Time Unit (derived)	TU	375,190.258663027 s

[a] spherical harmonic expansion radius from lp150q model

III. Periodic Orbit Generation

The symmetries typically associated with the RTBP or the zonal problem are no longer valid when considering an arbitrary Lunar gravity field. Thus, a full-dimensioned differential corrector is sought to find periodic orbits in the general non-symmetric case. The Jacobi integral, C, is a natural parameter to vary for generating families of solutions. Therefore, the constraint vector, **K**, consists of the periodicity conditions and the Jacobi integral target and is given in Eq. (14). The unknown vector, ξ_0, consists of each initial state variable except z_0, where the period and z dimensions are removed by setting z_0=0 and implicitly stopping the integration exactly at $z_T = 0$ (to machine precision), where T is the period. This discrete mapping technique is a proven strategy to reduce dimensions and is described in more detail in Refs [23,24,25,26].

$$
\mathbf{K} = \begin{pmatrix} \xi_T - \xi_0 \\ C - C_* \end{pmatrix}_{6\text{x}1}, \quad \xi = \begin{pmatrix} x & y & u & v & w \end{pmatrix}^{\mathrm{T}} \tag{14}
$$

Assume that an initial guess, ξ_0, in the vicinity of a solution yields a nonzero **K**. In order to drive the constraint vector to zero, a $\Delta\xi_0$ is sought that satisfies the linear system,

$$
\frac{d\mathbf{K}}{d\xi_0} \Delta\xi_0 = -\mathbf{K} \tag{15}
$$

* URL: http://naif.jpl.nasa.gov/naif/spiceconcept.html [cited 12 Mar 2006].
URL: ftp://naif.jpl.nasa.gov/pub/naif/generic_kernels/spk/planets/de405_2000-2050.bsp [cited 12 Mar 2006].
URL: ftp://naif.jpl.nasa.gov/pub/naif/generic_kernels/pck/pck00008.tpc [cited 12 Mar 2006].

Note that there are 5 unknowns and 6 constraints as stated in Eq. (15). In order to ensure a unique solution (given a non-singular Jacobian) many researchers reformulate the problem to have an equal number of constraints and unknowns [27,28]. On the contrary, in this study a least squares solution method allows for all of the constraints to be enforced regardless of the number of unknowns. Furthermore, singular value decomposition provides a simple solution to the problem of the degenerate Jacobian associated with a periodic orbit. The dimension of the null space of such a Jacobian is nonzero because any direction tangent to the solution leads again to a periodic solution. This degeneracy is compounded in the special case of a bifurcation periodic orbit, where there is an additional degenerate direction that leads to a new periodic orbit. The dimension reducing techniques discussed in Refs [26,27,28,29] deal effectively with the tangent degeneracy, but fail to address the special case of the bifurcation orbit. Unfortunately, all of the high-resonant Lunar orbits that are the subject of this study are bifurcation orbits. The singular value decomposition of the non-square Jacobian in Eq. (15) provides an elegant mechanism to reduce the system only in the degenerate directions, as opposed to the arbitrary directions proposed in Refs [27,28]. The 6x5 Jacobian has a singular value decomposition of the form

$$\frac{d\mathbf{K}}{d\boldsymbol{\xi}_0} = \mathbf{U}\mathbf{D}\mathbf{V}^{\mathsf{T}} \tag{16}$$

where **U** and **V** are square orthogonal matrices of dimension 6 and 5 respectively and **D** is a 6x5 matrix with non-negative entries on the diagonal and zeroes otherwise. See Ref. [30] for details on singular value decomposition. The psuedo-inverse of the Jacobian as indicated by the superscript '+' is given in Eq. (17) and leads to the least squares solution to the over-constrained system in Eq. (15). See Ref. [31] for a further description of a least squares application to differential orbit correction.

$$\left(\frac{d\mathbf{K}}{d\boldsymbol{\xi}_0}\right)^{+} = \mathbf{V}\mathbf{S}\mathbf{U}^{\mathsf{T}}, \quad S_{i,i} = \begin{cases} 1/D_{i,i} & \text{for} \quad D_{i,i} > \varepsilon \\ 0 & \text{for} \quad D_{i,i} < \varepsilon \end{cases} \tag{17}$$

The diagonal elements of **D** are called the singular values of the Jacobian. A singular matrix has at least one singular value of zero while an ill-conditioned matrix has at least one near-zero singular value. For practical computations, any singular value less than ε is considered zero as indicated in Eq. (17). For this study, ε values in the range of $10^{-4} \rightarrow 10^{-6}$ are found to be sufficient. Equation (18) gives the least squares solution to Eq. (15). Furthermore, as Ref. [30] explains, when one or more the singular values are zero (or < ε), then the solution given by Eq. (18) is the least squares solution with the smallest magnitude.

$$\Delta\boldsymbol{\xi}_0 = -\left(\mathbf{V}\mathbf{S}\mathbf{U}^{\mathsf{T}}\right)\mathbf{K} \tag{18}$$

Therefore, the problem associated with any degenerate directions is solved thru the simple selection of ε and the application of the Eq. (17). Furthermore, all of the constraints are active because there is no requirement for the Jacobian to be square. The Jacobian is calculated from

$$\frac{d\mathbf{K}}{d\boldsymbol{\xi}_0} = \begin{pmatrix} \dfrac{d\boldsymbol{\xi}_T}{d\boldsymbol{\xi}_0} - \mathbf{I}_{5\text{x}5} \\ \dfrac{dC}{d\boldsymbol{\xi}_0} \end{pmatrix}_{6\text{x}5} \tag{19}$$

$$\frac{d\boldsymbol{\xi}_T}{d\boldsymbol{\xi}_0} = \frac{\partial\boldsymbol{\xi}_T}{\partial\boldsymbol{\xi}_0} + \frac{\partial\boldsymbol{\xi}_T}{\partial T}\frac{\partial T}{\partial\boldsymbol{\xi}_0} \tag{20}$$

where the partial derivative of period with respect to the initial conditions is found from

$$\Delta z_T = \frac{\partial z_T}{\partial\boldsymbol{\xi}_0}\delta\boldsymbol{\xi}_0 + \dot{z}_T\delta T \tag{21}$$

Because the integrator implicitly stops on the *xy* plane, Eq. (21) can be solved with $\Delta z_T = 0$ giving

$$\frac{\partial T}{\partial\boldsymbol{\xi}_0} = -\frac{\partial z_T}{\partial\boldsymbol{\xi}_0}\frac{1}{\dot{z}_T} \tag{22}$$

Finally, Eq. (20) is rewritten as

$$\frac{d\boldsymbol{\xi}_T}{d\boldsymbol{\xi}_0} = \boldsymbol{\Phi}\left(T, t_0\right)_{i\neq 3,\, j\neq 3} - \frac{1}{\dot{z}_T}\dot{\boldsymbol{\xi}}_T \boldsymbol{\Phi}\left(T, t_0\right)_{i=3,\, j\neq 3} \tag{23}$$

where $\boldsymbol{\Phi}$ is the state transition matrix that provides the partial derivatives of the state from one time to another across a continuous trajectory. Thus,

$$\boldsymbol{\Phi}(t, t_0) = \partial \mathbf{X}(t) / \partial\, \mathbf{X}(t_0) \tag{24}$$

The state transition matrix is obtained by integrating the variational equations given in Eq. (25) along with Eq. (1). The calculation of the partial derivative in Eq. (25) is straight forward but tedious due to the complicated nature of **f** as described in Eqs. (2)-(9). For brevity, the equations are left out here.

$$\begin{aligned} \dot{\boldsymbol{\Phi}}(t, t_0) &= \left(\partial \mathbf{f} / \partial \mathbf{X}\right)\big|_t \, \boldsymbol{\Phi}(t, t_0) \\ \boldsymbol{\Phi}(t_0, t_0) &= \mathbf{I}_{6\text{x}6} \end{aligned} \tag{25}$$

To summarize, given that an initial guess, $\boldsymbol{\xi}_0$, is in the vicinity of a solution and yields a constraint violation **K**, the linearized first order correction is given by Eq. (18). Depending on the validity of the initial guess, it is often useful to scale the correction step in order to prevent any of the step directions from exceeding any of the user defined maximum step sizes. The process is iterated with the corrected guess until convergence as indicated by a constraint violation that is sufficiently small and is no longer reducing in length. The scalar normalized miss distance, d, is defined in Eq. (26) where $\|\ \|$ is the Euclidean 2-norm operator.

$$d = \left\|\mathbf{X}(t_f)_{i=1..3} - \mathbf{X}(t_0)_{i=1..3}\right\| \Big/ \left\|\mathbf{X}(t_0)_{i=1..3}\right\| + \left\|\mathbf{X}(t_f)_{i=4..6} - \mathbf{X}(t_0)_{i=4..6}\right\| \Big/ \left\|\mathbf{X}(t_0)_{i=4..6}\right\| + \left\|\left(C - C^*\right)/C^*\right\| \tag{26}$$

The stability of the converged solution is evaluated based on the full period state transition matrix, also known as the Monodromy matrix. It is well known that the eigenvalues of the Monodromy matrix for conservative autonomous systems occur in reciprocal pairs. Furthermore, tangent variations maintain periodicity. Therefore, the eigenvalues of the Monodromy matrix will have the form $\{\lambda_1, 1/\lambda_1, \lambda_2, 1/\lambda_2, 1, 1\}$. The complex stability indices are defined in Eq. (27) where $|b_i| \leq 2$ and b_i must be real for linear stability. For detailed discussions on the state transition matrix, the Monodromy matrix, and stability see Refs. [25, 32].

$$\begin{aligned} b_1 &= \lambda_1 + 1/\lambda_1 \\ b_2 &= \lambda_2 + 1/\lambda_2 \end{aligned} \tag{27}$$

IV. Families of Solutions

Periodic orbits in the perturbed RTBP enjoy the integral of motion, C, given in Eq. (10). The natural family of a single solution is found by successively seeking neighboring solutions for small fixed variations in C. For orbits close to the primary, energy variations generally lead to one of the two following effects: inclination variations with near-fixed eccentricity or eccentricity variations with near-fixed inclination that is commonly referred as the "critical inclination" [7,33]. The series solution expressions for the classic frozen orbits find singularities at this critical inclination. While the search for periodic orbits deal with the degenerate bifurcation case near this same inclination, methods such as the singular value decomposition approach described in this paper effectively deal with the degeneracy. For the high-altitude near-polar solutions, varying C across a family of orbits has the same effect as varying the average i. From a mission designer's perspective, i is an extremely important parameter when considering specific mission objectives and constraints.

For the near-circular inclined class of orbits sought in this study, the main characteristic that distinguishes one family from another is the integer ratio of spacecraft revolutions to body revolutions during a full period. In this paper, the number of spacecraft revolutions is varied while number of body revolutions is fixed to one. Accordingly, all solutions of an n-cycle family complete one period after exactly n spacecraft revolutions. The normalized period of each periodic solution is exactly one period of the body's revolution (2π) plus the total change in the longitude of the ascending node of the spacecraft orbit. The altitude, a second parameter of great importance to mission design, is controlled through the selection of n, where higher values of n correspond to lower altitudes.

To seek families of solutions that vary in C, the following algorithm is employed:

1. Select n, indicating the n-cycle family is sought.

2. Provide initial guess: Assuming a two-body orbit around a point mass Moon, calculate the initial conditions starting in the plane of the Moon's equator for a polar orbit that completes n revolutions during one Lunar revolution.

3. Use the initial guess and Eqs. (14)-(25) to converge on a periodic solution of the n-cycle family. Because this is the first member of the family, the Jacobi constant of the near-polar solution is unknown. Accordingly, the C constraint is removed from **K** in Eq. (14) and the dimensions of the following equations are appropriately modified. Thus, the inclination of the initial guess is polar, yet the solution is free to converge to any inclination. Generally, because the solution method is local, the algorithm converges to a near-polar periodic solution. Note, the near-polar solution is sought initially because the two body solution is a better guess at the near-polar inclinations and generally converges in the full perturbed RTBP model. For complex gravity fields like the Moon's, it may be necessary to parametrically solve several sub-problems where the first sub-problem includes the third-body effects, and each successive problem includes an increasingly complex gravity field and uses the initial conditions from the previous sub-problem.

4. Follow the initial near-polar solution in both directions for small variations in $\pm C$ until the user-supplied minimum or maximum is reached. A predictor-corrector scheme based on Eq. (18) is used for the continuation of a solution along its natural family. For the predictor step, the initial guess for each successive solution is found by solving Eq. (18) where the partial derivatives and C are evaluated along the previous periodic solution and **K** is $[0, 0, 0, 0, 0, C\text{-}C^*]^T$ where C^* is the new desired value for the Jacobi constant. The predicted initial condition is propagated for n cycles and is corrected using Eq. (18) and the full **K** from Eq. (14). The corrector step is iterated until convergence.

Families that vary in altitude yet maintain similar inclination are not continuous families because the generating parameter, n, is integer-valued. Nonetheless, these insightful groupings are found by repeating the first 3 steps of the algorithm for a desired range of n.

V. Example RGT Families and Orbits

For large variations in altitude, near-polar RGT solutions are sought for n values of 73 to 328 cycles at increments of 15. Figure 2 shows the results where each solution is initiated with a 90.5^o two body circular orbit. As the Jacobi integral is left unconstrained, the solutions are free to evolve to any inclination (although a max-step size of 10 km in position and .1 km/s in velocity constrains the solution to stay in the vicinity of the guess). For these near-polar solutions, as the minimum altitude decreases from 3319 km to 39 km, the average eccentricity increases from ~0 to ~0.04. Note, the miss distance, d, is consistently near 10^{-12} normalized units, indicating the initial and final conditions are equivalent to approximately 12 significant digits. Of the most important observations from Figure 2 is the unstable to stable transition that occurs near 168 cycles at an approximate altitude of ~1200 km as indicated by the boundary where both stability indices equal 2. Also, note that the average ratio of the magnitudes of the harmonic to the tidal perturbing forces is unity at an approximate altitude of ~2000 km.

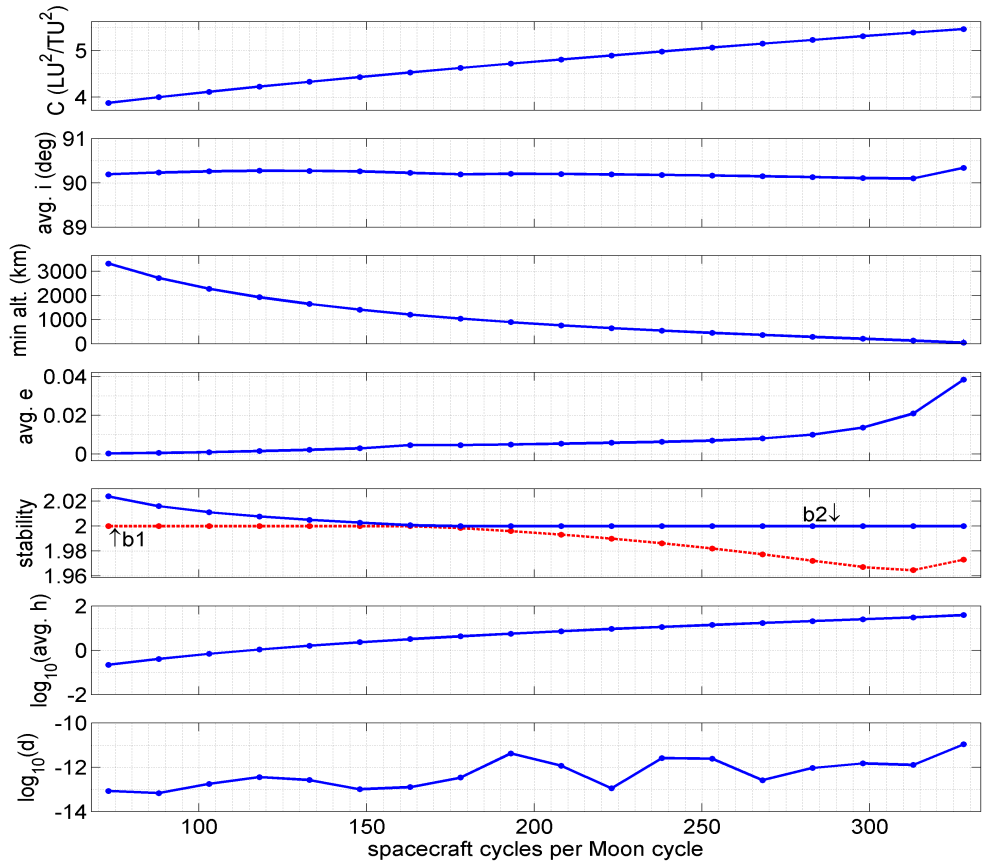

Figure 2. Characteristics of near-polar RGT solutions for *n*-cycles of 73 to 328. *d* is the periodicity precision defined in Eq. (26). *h* is the ratio of the magnitude of the Moon's harmonic acceleration to the tidal acceleration due to the Earth.

For a given *n*-cycle orbit from Figure 2, its natural family is found for small variations in *C*. As examples, the high altitude, 73-cycle and the low altitude, 328-cycle natural families are presented in Figure 3 and Figure 4. Figure 3 shows the high-attitude family consists of mildly unstable orbits with very low eccentricities for a wide range of inclination centered at 90° while the family ends in both *C* directions with stable highly eccentric impact orbits. All of the near-circular orbits are mildly unstable where the maximum instability is represented by the shallow maximum in b_2 that occurs near 90°. The eccentricities grow rapidly in both directions as the family passes through the critical inclinations of approximately 43° and 139° where both stability indices equal 2. Outside of the critical points, a reflection in inclination occurs until the family ends with stable impact orbits of $\{C,i,e\}\sim\{3.8474\ \mathrm{LU}^2/\mathrm{TU}^2, 125^\circ, 0.656\}$ and $\{3.9005\ \mathrm{LU}^2/\mathrm{TU}^2, 55.6^\circ, 0.644\}$. The existence and location of the stable eccentric orbits are consistent with the frozen orbits around the Earth and Moon discussed in Refs. [2,5,7,16,17,11].

It is worth noting that different 73-cycle families of RGT orbits are found by starting near the direct or retrograde planar orbits. These families begin as stable near-circular orbits and reflect in *C* near the critical inclination where they transition to stable eccentric orbits with closest approach over the southern Lunar pole ($\omega\sim-90^\circ$). These orbits have the opposite orientation from the eccentric orbits of the family shown in Figure 3 where the closest approach is over the northern pole ($\omega\sim90^\circ$). Although the search method is applicable for periodic families of all types, the attention of this study is focused on the families centered on the polar inclinations because of their favorable global coverage.

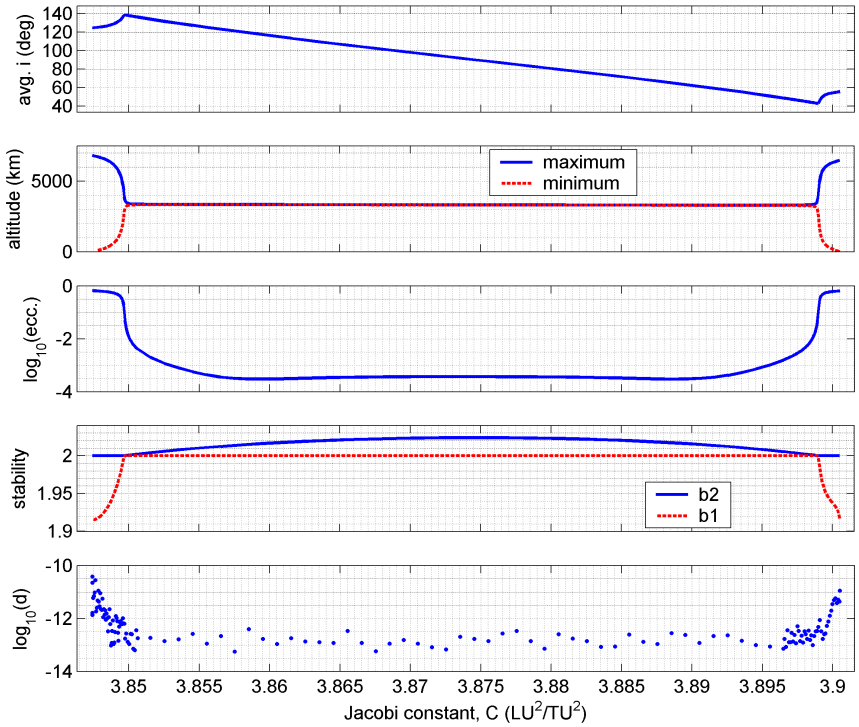

Figure 3. Characteristics of the 73-cycle RGT family.

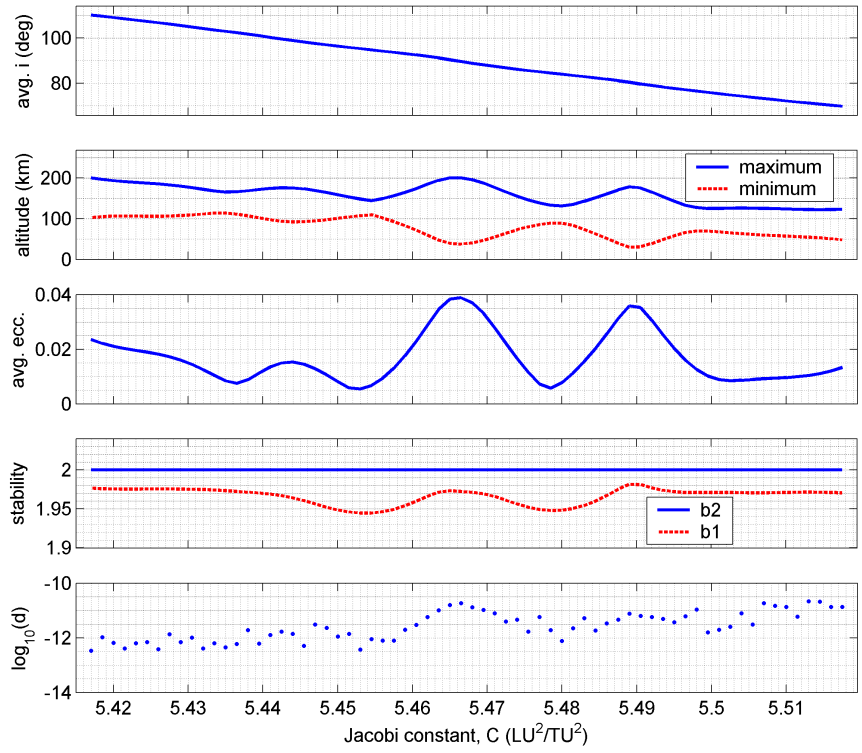

Figure 4. Characteristics of the 328-cycle RGT family.

Figure 4 shows the evolution of the low altitude 328-cycle natural family. The evolution of the eccentricity vs. inclination curve finds general agreement with the lower-order frozen Lunar orbits found in Ref. [2,3,4,5,6] noting that the best agreement is with those reported in Ref. [4] based on the LGM0281 gravity field. The stability indices from Figure 4 show linear stability for the full range of near-polar inclinations. The highly non-spherical gravity field manifests through large variability in the average eccentricities. There are two noteworthy minimums occurring near 85° and 95° while the most polar orbit finds a maximum eccentricity of ~0.04. The near-zero eccentricity solutions are consistent with the frozen Lunar orbits found in the literature. However, the inclusion of the third-body and the non-zonal terms destroys the existence of the exactly circular frozen orbits. The smallest variation in altitude occurs at an average inclination of 94.8° with minimum and maximum altitudes of 110 and 144 km. The higher order effects of including the non-zonal terms as well as the third body perturbations are further appreciated in the loss of symmetry with respect to i=90°. While symmetry remains to first order as the two-body zonal problem predicts [2,7], the peak in eccentricity that occurs near i = 80° is more than twice as high as the peak that occurs at i=100°. This lack of symmetry is also evident in the altitude and stability plots.

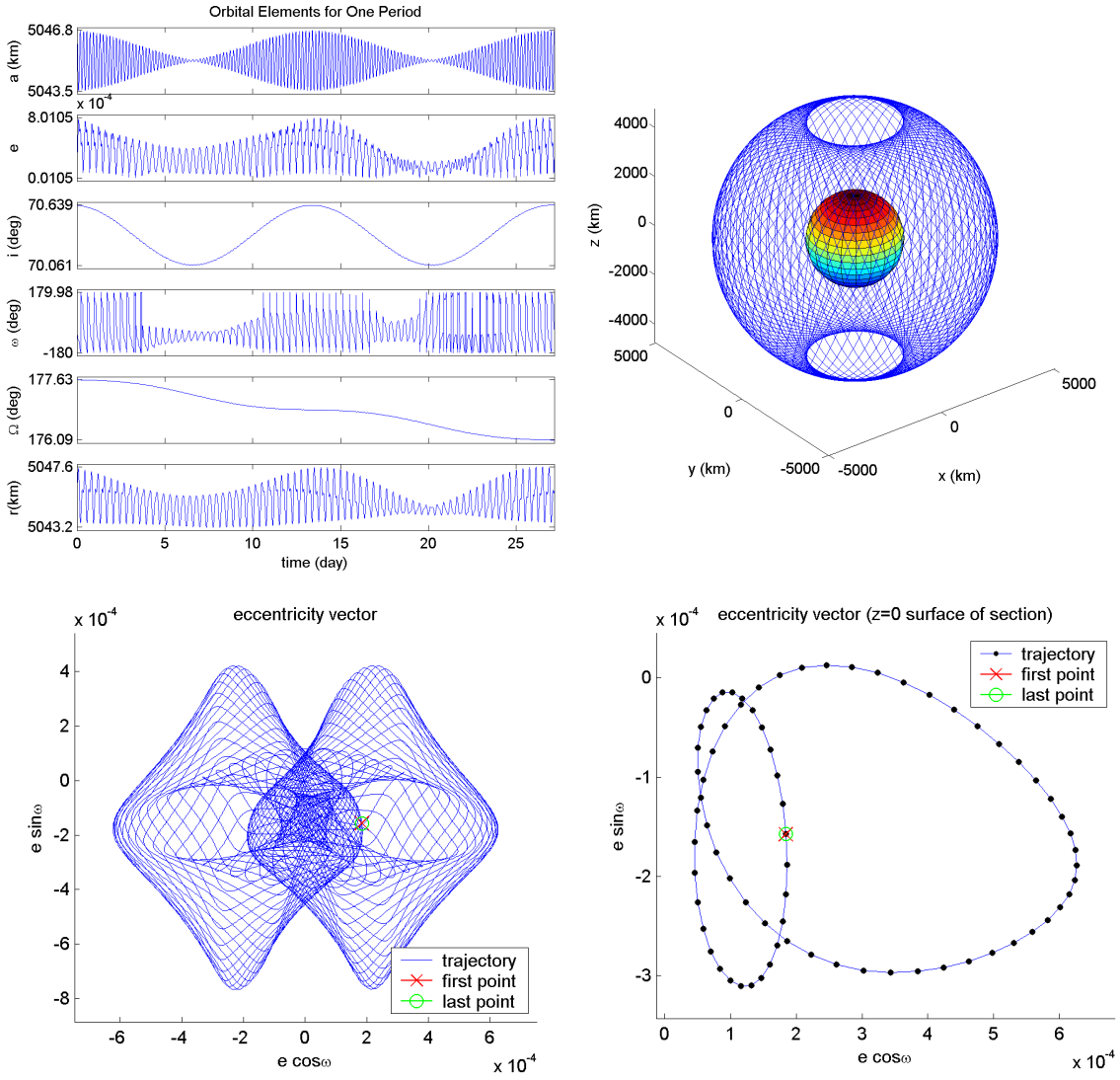

Figure 5. Characteristics of example near-circular 73-cycle RGT periodic orbit (Orbit A)

Figure 5 - Figure 7 illustrate three example point solutions from the 73- and 328-cycle families. These solutions are termed Orbits A, B, and C respectively. The initial conditions and other characteristics for the example solutions are given in Table 2. Note that the degeneracy associated with one of the stability indices always being 2 indicates that the solutions are not necessarily unique. Thus, qualitatively similar solutions with minor differences in initial conditions are possible to achieve despite having the same *C* value. This is consistent with the findings in Ref. [17]. While all RGT orbits are periodic in each of the six rotating Cartesian coordinates by definition, Figure 5 - Figure 7 show that each of the orbital elements are periodic except the longitude of ascending node, Ω. (It was noted previously that $\Delta\Omega = T - 2\pi$.) The short period oscillations seen in the orbital elements of Orbits A-C result from each spacecraft revolution, while the long period oscillations result from the variability of the perturbing force field as the orbit plane rotates around the body. The large erratic variations in the long period motion of Orbit C, the low-altitude 328-cycle orbit, are indicative of the notoriously lumpy Lunar gravitational field. As further evidence, the argument of periapse, while centered on the $\omega \sim -90^o$ as the zonal problem predicts, appreciates non-trivial variations of $\pm 17^o$ during the course of one period. These large variations in argument of periapse are common to all members of the 328-cycle family. Note that the mean is near $\omega \sim -90^o$ for all of the orbits considered in Figure 4 except those in the inclination ranges associated with the non-polar rises in eccentricity ($75^o < i < 84^o$ and $95^o < i < 103^o$) where the mean is shifted to $\omega \sim 90^o$. The presence of step function shifts in mean ω is consistent with results from Refs. [2,4] although the exact locations vary because of the different gravity fields and levels of model fidelity.

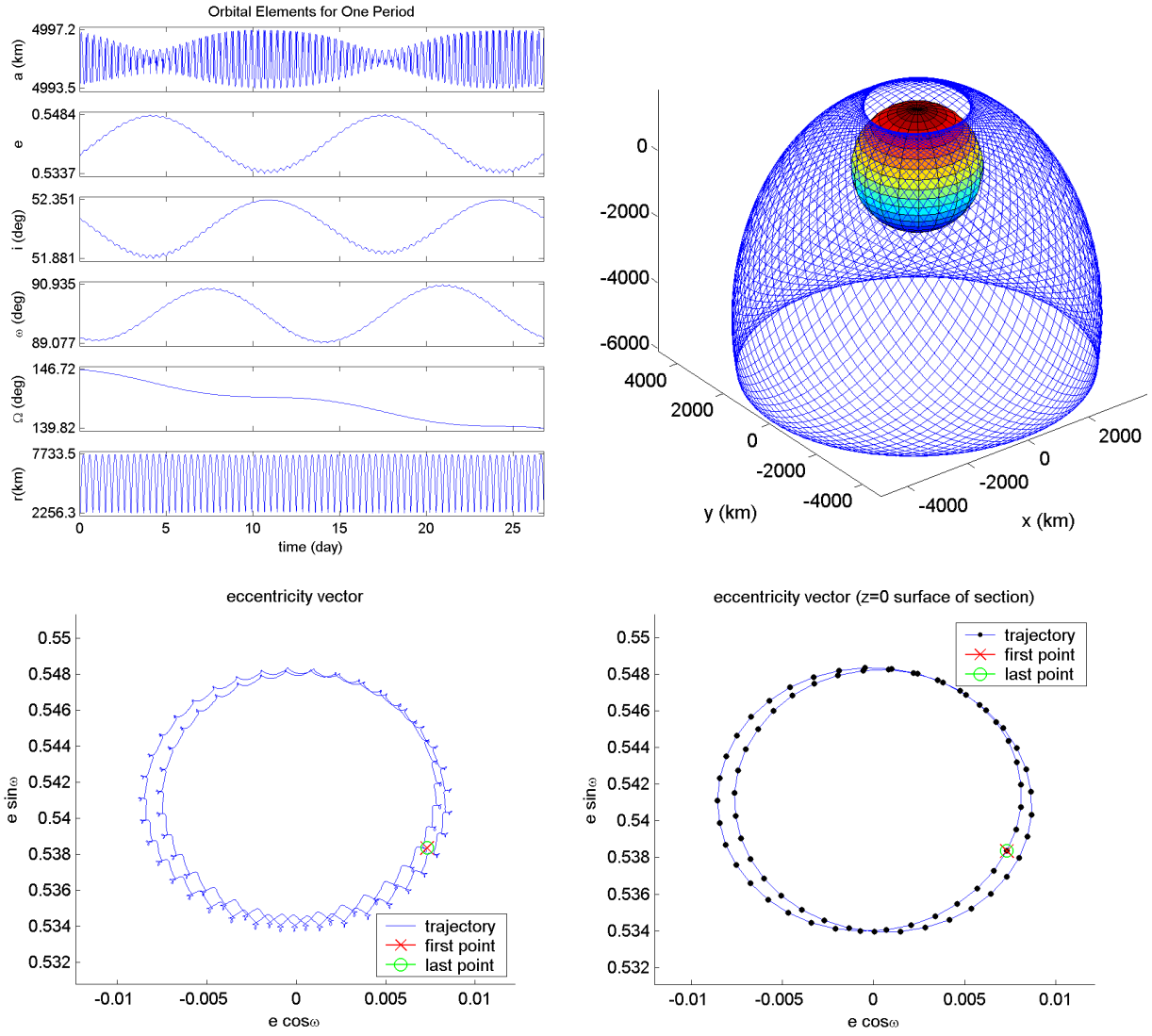

Figure 6. Characteristics of example eccentric 73-cycle RGT periodic orbit (Orbit B)

Table 2. Example orbit data (z_0=0, v_0=-ω_0)

Property	Units	Orbit A (73-cycle)	Orbit B (eccentric 73-cycle)	Orbit C (328-cycle)
x_0	LU	-1.311519120505E-02	-7.660645625403E-03	-4.498948742093E-03
y_0	LU	5.435394815081E-04	5.028162133106E-03	-1.731769313131E-03
u_0	LU/TU	-1.281711107594E-02	1.327777508469E-01	-6.203996010078E-02
v_0	LU/TU	-3.056086111584E-01	-9.233621714500E-01	7.000280770869E-02
w_0	LU/TU	9.077797920947E-01	9.132878998189E-01	1.588813067177E+00
C	LU^2/TU^2	3.885779329543E+00	3.899472252543E+00	5.460492546479E+00
a_0	km	5.046738218681E+03	4.996647749602E+03	1.861791339407E+03
e_0	-	2.425326521133E-04	5.384086098625E-01	2.110475283361E-02
i_0	deg	7.063797094157E+01	5.220698531621E+01	9.298309204740E+01
ω_0	deg	-4.048674547795E+01	8.922084663298E+01	-7.839337618501E+01
Ω_0	deg	1.776268201967E+02	1.467205983429E+02	-1.589469097527E+02
T	day	2.716778449596E+01	2.676187032099E+01	2.735409767795E+01
avg. i	deg	70.4	52.1	92.5

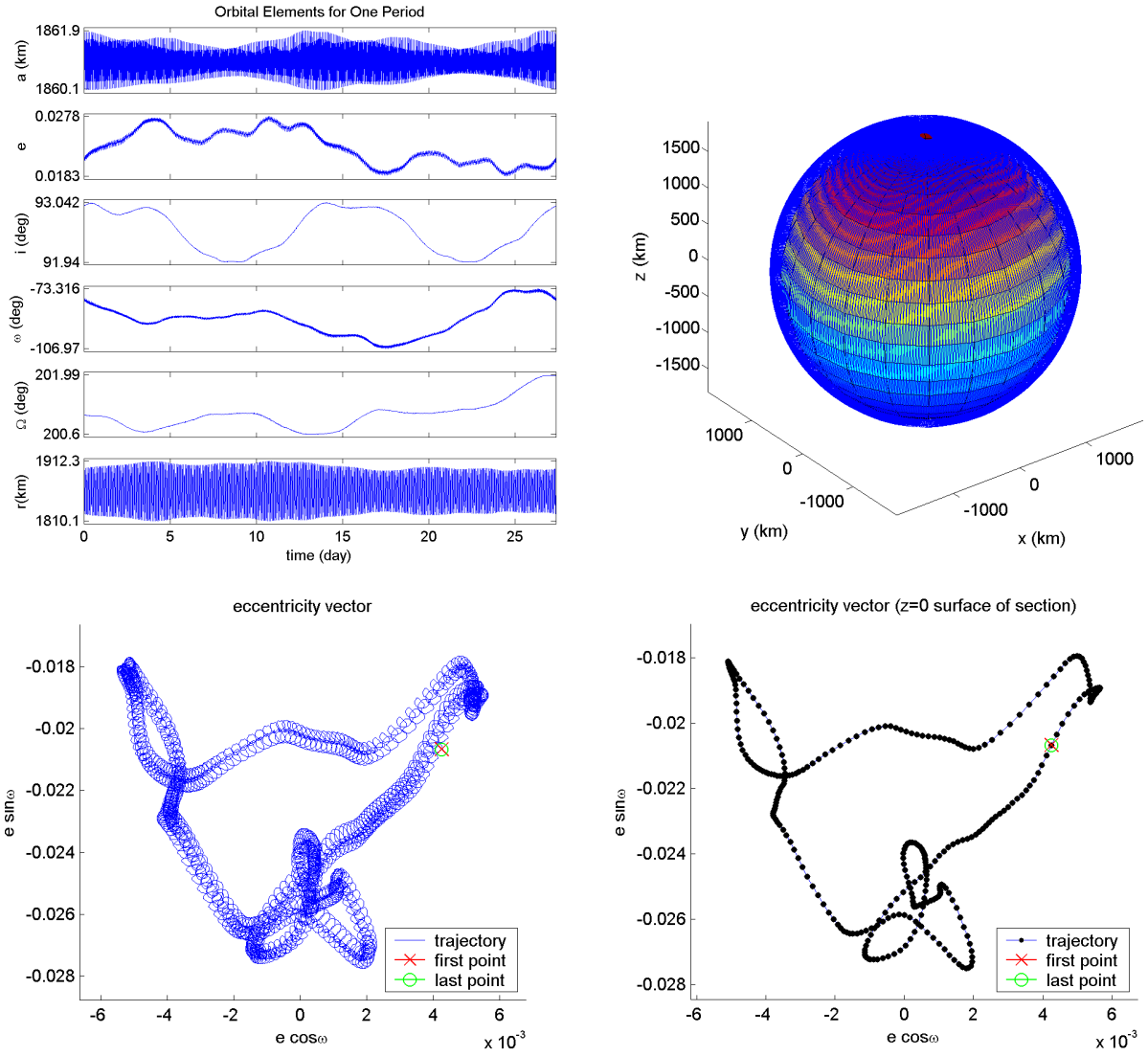

Figure 7. Characteristics of example near-circular 328-cycle RGT periodic orbit (Orbit C)

The bottom rows of Figure 5 - Figure 7 show the evolution of the tip of the eccentricity vector for the example RGT solutions. The full trajectory path is given as well as a discrete map illustrating the *xy*-plane crossings. These meandering paths close after one period and repeat indefinitely for a spacecraft that remains on an RGT solution. The eccentricity vector plots are useful tools for the visualization and analysis of the long-term stability of frozen and near-frozen orbits [2,3,6,7,9,10,13,12,34].

The orbit propagations are performed using a Runge-Kutta 7(8) integrator and the step sizes are chosen such that the Jacobi constant, *C*, is conserved to at least 13 digits over the course of a full period. The computational times per iteration of a point solution are ~20 and ~90 seconds on 3.2 GHz Xeon processor for the 73-cycle and 328-cycle trajectory respectively.

VI. Long-Term Propagations

A numerically propagated orbit suffers from round-off and truncation error that emulate small perturbations to a spacecraft trajectory. For an unstable reference orbit, these perturbations grow with a characteristic time directly related to the magnitude of the largest eigenvalue of the Monodromy matrix (and consequently the largest stability index). A stable orbit, on the other hand, will generally be robust to the small numerical perturbations in the context of long-term stability. Figure 8 illustrates a long propagation of the mildly unstable high altitude Orbit A. While the RGT condition is nearly maintained for the first 11 years, the eccentricity grows exponentially and finally suffers a Lunar impact after 15.7 years. Twenty-year propagations of the stable eccentric Orbit B and the stable low-altitude Orbit C yield repeated eccentricity vector paths that are indistinguishable from those illustrated in Figure 6 and Figure 7.

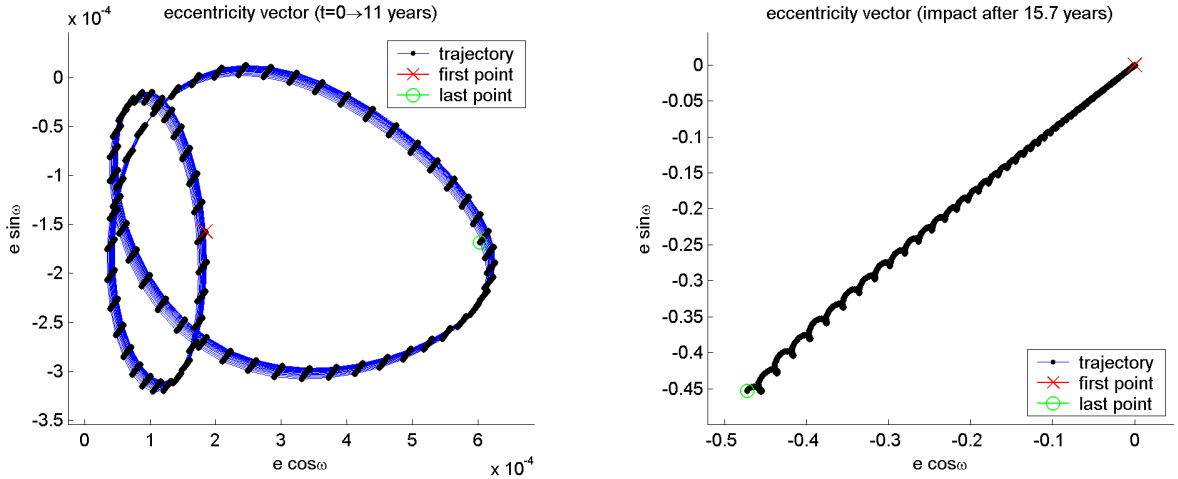

Figure 8. Eccentricity vector at the *xz*-plane crossings of a long propagation (RTBP plus 50x50 Lunar gravitational model) of the mildly unstable 73-cycle Orbit A. Left: the first 11 years. Right: the full 15.7 year propagation ending at impact. Note the difference in axis scales.

While the RTBP represents the motion of the Moon and the Earth well to first order, the effects of considering a more realistic model represent perturbations to the system that are many orders of magnitude greater than those that result from numerical error. This is especially true at the Moon where its mean eccentricity is far from zero at 0.06 and Solar perturbations are significant. As an example of the Solar effects, the Lunar true period varies on the order of ±3 hours over the course of several periods. To test the validity of the solutions in the context of these realistic perturbations, long-term propagations using the ephemeris force model (described in an earlier section) are performed. An arbitrary epoch of 12:00 1-1-2010 (Julian Date = 2455198.0) is used for the initial conditions.

Figure 9 - Figure 11 illustrate ephemeris propagations for each of the example Orbits A-C respectively. The left side of each figure shows the full path of the eccentricity vector for the first period while the right side gives the *xz*-plane crossings for the long runs. The initial conditions from Table 2 are applied in the IAU body-fixed Moon frame [22] at epoch. The reported e and ω values are expressed in the ecliptic J2000 frame. While the eccentricity vector path of the first period of Orbit A is similar to the perturbed RTBP version (see bottom left of Figure 5), the long-term instability is greater in the real ephemeris and the orbit suffers a Lunar impact after 5.57 years. Note that the ephemeris propagation of Orbit A falls off of the frozen conditions in a different direction than the perturbed RTBP propagation.

As evidenced by the non-closed eccentricity vector path after the first period, the left side of Figure 10 shows the inability of Orbit B to maintain the RGT orbit in the ephemeris model. The radius of the stability region associated this stable eccentric orbit in the perturbed RTBP appears too small to overcome the ephemeris perturbations. Despite falling off of the RGT path, the orbit does find long-term stability as seen in the long period libration in the $e\omega$ plane with large amplitudes in Δe. This motion is consistent with the dynamics predicted by the simpler RTBP unperturbed by a non-spherical Lunar gravity field [11].

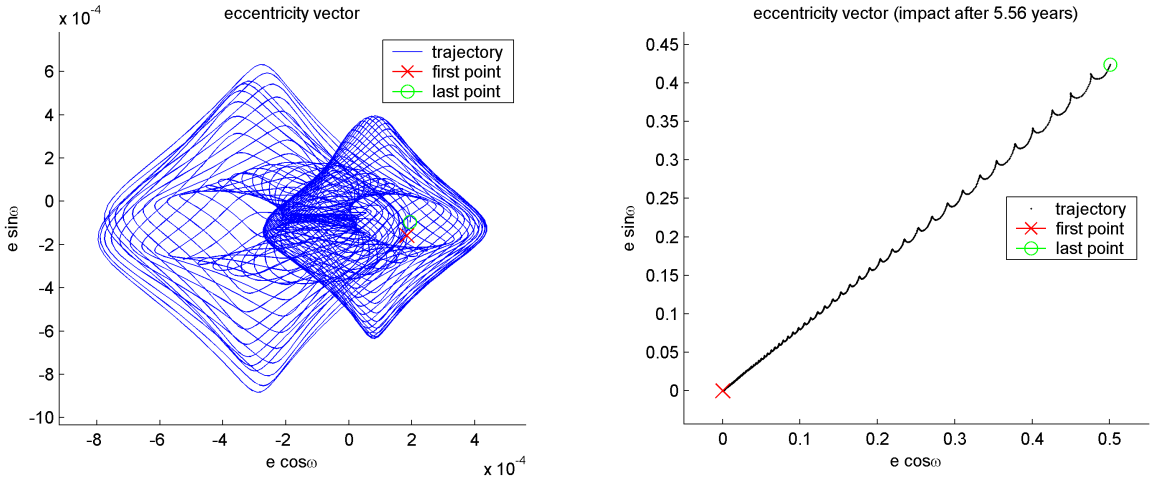

Figure 9. Ephemeris propagation of the mildly unstable 73-cycle Orbit A. Left: one period (compare to the bottom left of Figure 5). Right: 5.56 year propagation ending with impact.

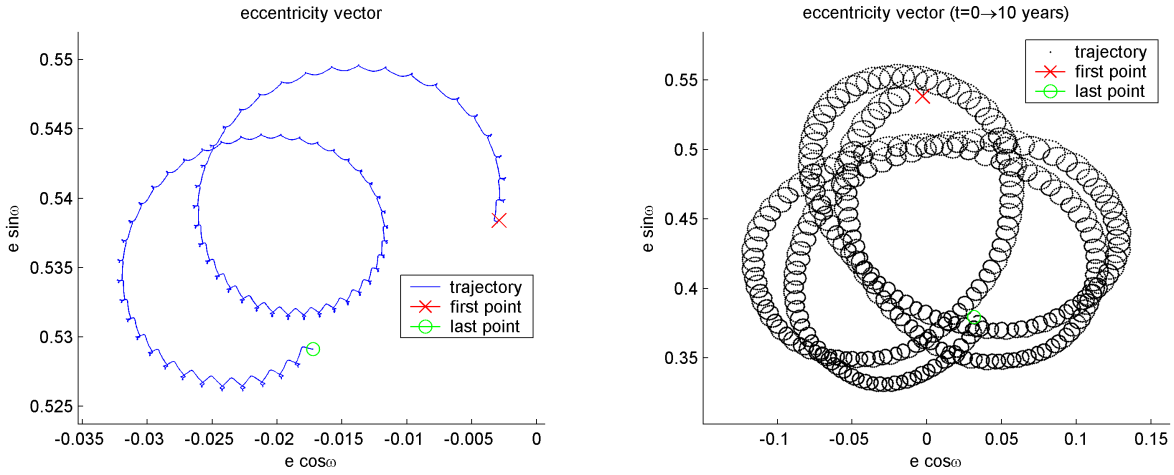

Figure 10. Ephemeris propagation of the stable eccentric 73-cycle Orbit B. Left: one period (compare to the bottom left of Figure 6). Right: Surface of section (z=0) map of 10 year propagation.

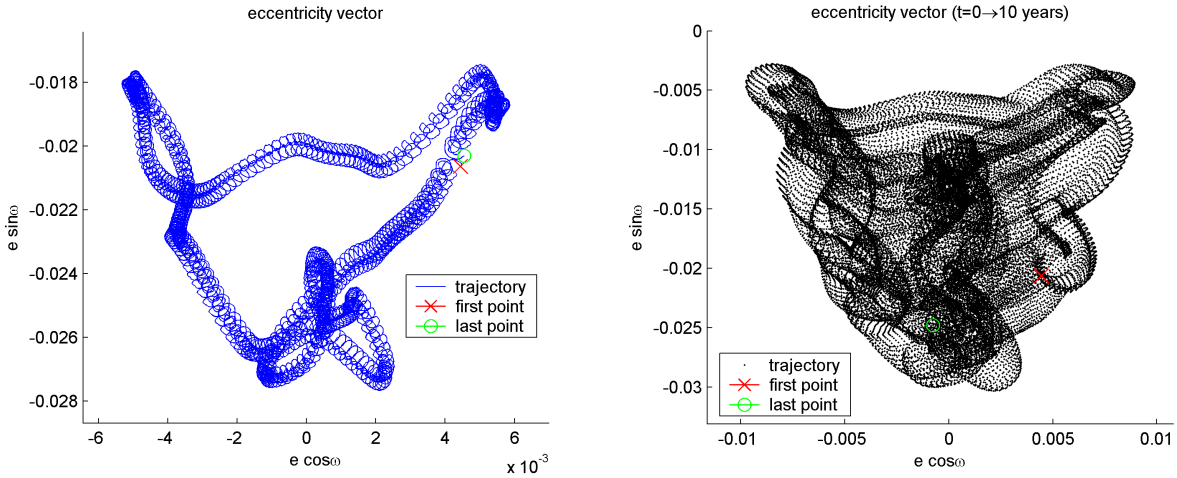

Figure 11. Ephemeris propagation of the stable 328-cycle Orbit C. Left: one period (compare to the bottom left of Figure 7). Right: Surface of section (z=0) map of 10 year propagation.

As expected, the agreement is qualitatively better for the case of the low-altitude near-circular Orbit C where the assumptions of the RTBP play a much lesser role because the non-spherical gravity perturbations at this altitude are ~39 times larger (from Figure 2) than the tidal perturbations due to the Earth. The first period of the ephemeris propagation maps an almost identical eccentricity vector path to that from the invariant model. While the remaining ~132.4 periods do not replicate the pattern exactly, the right side of Figure 11 shows that the orbit librates in the $e\omega$ plane with similar magnitudes. Therefore, the low altitude, near-circular, near-polar Orbit C enjoys long-term stability in an ephemeris model for at least 10 years.

VII. Gravity Field Degree And Order

As mentioned previously, a sensitivity study in Ref. [3] on the affect of the gravity field degree on a low-altitude Lunar orbiter indicates the dynamics appreciably change as the degree increases for up to at least a 50 degree field. These claims are substantiated in Ref. [18] and led to the use of the truncated 50x50 field for the bulk of the present study. However, it is natural to question the sensitivity of the current results to the degree and order of the truncation. Accordingly, Figure 12 presents the same 328-cycle family of the RGT orbits for a variety of different truncated versions of the lp150q gravity field. A full degree and order field and a zonal only version are considered for degrees of 7, 20, and 50. In general, the results are consistent with the previous research that shows high sensitivity to the inclusion of the higher degree terms. All three of the degrees find maximums in e near i=90°. For the inclination range considered, the degree 20 and 50 fields lead to four minimums in e while the 7 degree fields find only 2 minimums. The locations and values of the extrema vary for each field considered.

The effects of the non-zonal terms are easily seen in Figure 12 by comparing the curves of common degree. In each case, the zonal-only curves closely approximate the full degree and order curves. The comparison does however reveal a positive shift in eccentricity for the non-polar full degree and order families. The exactly circular solutions from the zonal-only problem are destroyed by this shift in eccentricity. The magnitude of the shift appears to increase with degree noting the difference in some cases is as large as $\Delta e \sim 0.01$. The lack of symmetry between the direct and retrograde periodic orbits is primarily a consequence of the third-body influence and is appreciated when the perturbation is formulated in orbital elements [34]. The non-zonal gravitational terms further destroy the symmetry about the polar orbit.

The increase in fidelity of using a full degree and order field does however come at a substantial cost. Including all of the computations, the run-time per iteration for a solution in the 50x50 field increases by a factor of ~30 compared to the zonal only 50x0 field. Despite the speed penalty, the generation of the high-fidelity 328-cycle family in a 50x50 field requires one overnight job on a single 3.2 GHz Xeon processor. In contrast, the lower-fidelity families consisting of the zonal terms only (plus the third-body effects) are generated in just a few minutes

enabling rapid analysis for a variety of mission design applications. Note that the higher altitude orbits are intrinsically faster to generate because each period requires fewer cycles. Furthermore, they are less susceptible to the higher order effects of the non-zonal terms. Therefore, the high-altitude orbits that remain far from the Lunar surface are sufficiently modeled using the zonal terms only. It is emphasized that the computational run-time is a linear function of the number of cycles required to close a given RGT orbit. The slow rotation rate of the Moon requires over 300 cycles for the low altitude RGT orbits while the low altitude RGT orbits at Europa, for example, require approximately 40 cycles [13]. Thus, the run-times found in the current RGT Lunar application are generally an order of magnitude greater than those expected from analogous applications at most other celestial bodies of interest.

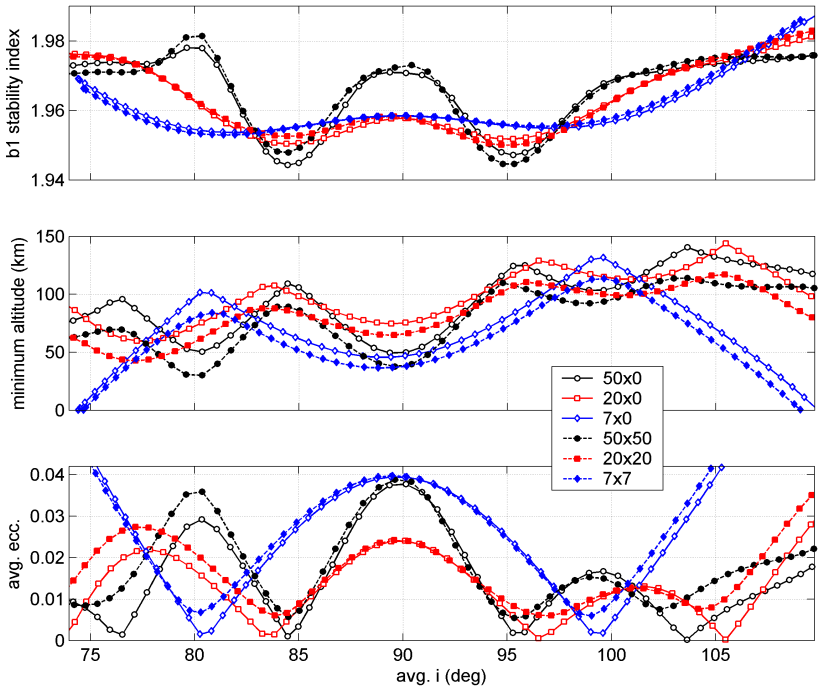

Figure 12. The 328-cycle RGT family based on 6 truncated versions of lp150q gravity field.

VIII. Conclusions

This study presents an alternative systematic method for finding long-life orbits around the Moon. The RGT periodic orbits are demonstrated and characterized in the Earth-Moon Restricted Three Body model perturbed by a high resolution Lunar gravity field. The families of periodic orbits are found to be subsets of the classic frozen Lunar orbits from the literature. However, the RGT orbits represent higher order solutions because they additionally include the unaveraged equations of motion, the non-zonal harmonic terms, and the tidal forces from the RTBP. Because these solutions exist for most altitudes and inclinations, and they are not limited to small eccentricity, Moon RGT orbits are of direct application to a variety of missions. From a trajectory designer's perspective, the RGT search algorithms are implemented in a general toolkit that is easily adaptable for any gravity field and any mass ratio. Furthermore, little or no domain expertise is required.

The described differential correction technique uses singular value decomposition to remove the degeneracies that typically plague full-dimensioned searches for periodic orbits. The method is systematic and shown to be efficient for finding single solutions and following families of solutions. The technique is applicable for all types of periodic orbit searches: symmetric and asymmetric, not limited to the class of high-resonant orbits studied here.

The better agreement between the invariant model and ephemeris occurs for low altitude orbits, where a high degree and order Selene-potential is included in the invariant model. As altitude increases and approximations of the RTBP deteriorate, the ephemeris solutions are less accurately predicted by the invariant model and require further tuning to optimize lifetimes. For the higher altitude orbits, the general techniques described in this study will find better application in planetary moon systems that are more accurately modeled with the RTBP.

The low-altitude, near-circular families are shown to be stable for a wide range of useful altitudes and inclinations. The solutions find strong enough resonance in the highly non-spherical Lunar gravity field to overcome the ephemeris perturbations and thus enjoy long lifetimes in the realistic model. This long-term stability and systematic methodology makes the RGT orbits immediately applicable to current and planned Lunar exploration missions requiring orbiters with close surface proximity.

Acknowledgments

The authors thank Alex Konopliv for contributing discussions and references. M. L. thanks support from projects ESP2004-04376 and ESP2005-07107 of the Spanish Government. Part of this work was carried out at the Jet Propulsion Laboratory, California Institute of Technology, under a contract with the National Aeronautics and Space Administration.

References

[1] "The Vision for Space Exploration," National Aeronautics and Space Administration Publication, NP-2004-01-334-HQ, February, 2004.

[2] Cook, Richard, "The Long-Term Behavior of Near-Circular Orbits in a Zonal Gravity Field", Paper AAS 91-463, AAS/AIAA Astrodynamics Specialist Conference in Durango, Colorado, August 1991.

[3] Konopliv, A.S., Sjogren, W.L., Wimberly, R.N., Cook, R.A., Vijayaraghavan, A., "A High Resolution Lunar Gravity Field and Predicted Orbit Behavior", Paper AAS 93-622, AAS/AIAA Astrodynamics Specialist Conference in Victoria, B.C., Canada, August 1993.

[4] Park, S.Y., Junkins, J.L., "Orbital Mission Analysis for a Lunar Mapping Satellite", *Journal of the Astronautical Sciences*, Vol. 43, No. 2, 1995, pp. 207-217.

[5] Elipe, A., Lara, M., "Frozen Orbits about the Moon," *Journal of Guidance and, Control*, Vol. 26, No. 2, 2003, pp. 238-243.

[6] Folta, D., Galal, K., Lozier, D., "Lunar Prospector Frozen Orbit Mission design", paper AIAA-1998-4288, Astrodynamics Specialist Conference and Exhibit, Boston, MA, August 1998.

[7] Coffey, S., Deprit, A., and Deprit, E., "Frozen Orbits for Satellites Close to an Earth-Like Planet," *Celestial Mechanics and Dynamical Astronomy*, Vol. 59, No. 1, 1994, pp. 37–72.

[8] Rosborough, G.W., Ocampo, C.A., "Influence of Higher Degree Zonals on the Frozen Orbit Geometry," Paper AAS 91-428, AAS/AIAA Astrodynamics Specialist Conference in Durango, Colorado, August 1991.

[9] Paskowitz, M. E., Scheeres, D.J., "Transient Behavior of Planetary Satellite Orbiters", Paper AAS 05-358, AAS/AIAA Astrodynamics Specialist Conference in Lake Tahoe, California, August 2005.

[10] Broucke, R.A., "Long-Term Third-Body Effects via Double Averaging," *Journal of Guidance and, Control*, Vol. 26, No. 1, 2003, pp. 27-32.

[11] Ely, T., "Stable Constellations of Frozen Elliptical Inclined Lunar Orbits," *Journal of the Astronautical Sciences*, Vol. 53, No. 3, 2005, pp. 301-316.

[12] Ely, T., "Constellations of Elliptical Inclined Lunar Orbits Providing Polar and Global Coverage," paper AAS 05-343, AAS/AIAA Astrodynamics Specialist Conference, Lake Tahoe, California, August 2005.

[13] Lara, M., Russell, R.P., "On the Design of a Science Orbit about Europa," Paper AAS 06-168, AAS/AIAA Space Flight Mechanics Meeting, Tampa, Florida, 2006.

[14] Lara, M., Russell, R.P., Villac, B., "On Parking Solutions Around Europa", Paper AAS 05-384, AAS/AIAA Astrodynamics Specialist Conference in Lake Tahoe, California, August 2005.

[15] Gomez, G., Lara, M., Russell, R., "A Dynamical Systems Approach to the Design of the Science Orbit around Europa," Paper ISTS 2006-d-02, 19th International Symposium on Space Flight Dynamics, Kanazawa, Japan, 2006.

[16] Lara, M., "Searching for Repeating Ground Track Orbits: A Systematic Approach", *The Journal of the Astronautical Sciences*, Vol. 47, 1999, pp. 177–188.

[17] Lara, M., "Repeat Ground Track Orbits of the Earth Tesseral Problem as Bifurcations of the Equatorial Family of Periodic Orbits", *Celestial Mechanics and Dynamical Astronomy*, Vol. 86, No. 2, 2003, pp 143-162.

[18] Roncoli, R. B., "Lunar Constants and Models Document," JPL D-32296, Jet Propulsion Laboratory, Pasadena, California, September, 2005. Section 2.1.

[19] Tapley, B.D., Schutz, B.E., Born, G.H., *Statistical Orbit Determination*, Elsevier Academic Press, Burlington, MA, 2004. Section 2.3.
[20] Lambeck, K., *Geophysical Geodesy*, Clarendon Press, Oxford, 1988. Sec. 2.2.
[21] Standish, E. M., *JPL Planetary and Lunar Ephemerides*, CD-ROM, Willman-Bell Inc., Richmond, VA, 1997.
[22] Seidelmann, P.K., Abalakin, V.K., Bursa, M., Davies, M.E., Bergh, C. de, Lieske, J.H., Oberst, J., Simon, J.L., Standish, E.M., Stooke, P., Thomas, P.C., "Report of the IAU/IAG Working Group on Cartographic Coordinates and Rotational Elements of the Planets and Satellites: 2000," *Celestial Mechanics and Dynamical Astronomy*, Vol. 82, Issue 1, 2002, pp. 83–111.
[23] Howell, K. "Three-dimensional, Periodic, 'Halo' Orbits," *Celestial Mechanics*, Vol. 32, 1984, pp. 53–71.
[24] Ocampo, C. A., "Trajectory Optimization for Distant Earth Satellites and Satellite Constellations," Ph.D. Thesis, Department of Aerospace Engineering, University of Colorado, Oct. 1996. pp. 18,53.
[25] Russell, R. P., "Global Search for Planar and Three-dimensional Periodic Orbits Near Europa," paper AAS 2005-290, AAS/AIAA Astrodynamics Specialist Conference, Lake Tahoe, California, August 2005.
[26] Bellerose, J., Scheeres, D.J., "Periodic Orbits in the Full Two-Body Problem," paper AAS 06-169, presented at the AAS/AIAA Space Flight Mechanics Meeting, Tampa, Florida, 2006.
[27] Szebehely, V., *Theory of Orbits. The Restricted Problem of Three Bodies*, Academic Press, New York, 1967. Section 8.4.
[28] Siegel, C.L., Moser, J.K., *Lectures on Celestial Mechanics*, Springer-Verlag, New York, 1971. pp. 139-151.
[29] Lara, M., and Pelaez, J., "On the Numerical Continuation of Periodic Orbits: An Intrinsic, 3-Dimensional, Differential, Predictor-Corrector Algorithm," *Astronomy and Astrophysics*, Vol. 389, February 2002, pp. 692–701.
[30] Lay, D.C., *Linear Algebra and its Applications, Second Edition*, Addison-Wesley, Reading, Massachusetts, 2000, pp. 466-475.
[31] Gomez, G., Llibre, J., Martinez, R., Simo, C., *Dynamics and Mission Design Near Libration Points. Vol. I Fundamentals: The Case of Collinear Libration Points*, World Scientific Monograph Series in Mathematics, Vol. 2, World Scientific, Singapore, 2001. pg. 94.
[32] Broucke, R., "Stability of Periodic Orbits in the Elliptic, Restricted Three-Body Problem," *AIAA Journal*, Vol. 7, No. 6, 1969, pp. 1003-1009.
[33] Jupp, A.H., "The Critical Inclination: 30 Years of Progress," *Celestial Mechanics*, Vol. 43, 1988, pp. 127-138.
[34] Scheeres, D.J., Guman, M.D., "Stability Analysis of Planetary Satellite Orbiters: Application to the Europa Orbiter," *Journal of Guidance and, Control*, Vol. 24, No. 4, 2001, pp. 778-787.